



## **AIAA 2002-2794**

# Uncertainty of Videogrammetric Techniques used for Aerodynamic Testing

A. W. Burner, Tianshu Liu, Richard DeLoach  
NASA Langley Research Center  
Hampton, VA

**22nd AIAA Aerodynamic  
Measurement Technology and  
Ground Testing Conference**  
24-26 June 2002/St. Louis, Missouri

## Uncertainty of Videogrammetric Techniques used for Aerodynamic Testing

A. W. Burner\*, Tianshu Liu†, Richard DeLoach‡  
 NASA Langley Research Center  
 Hampton, VA 23681-2199

### ABSTRACT

The uncertainty of videogrammetric techniques used for the measurement of static aeroelastic wind tunnel model deformation and wind tunnel model pitch angle is discussed. Sensitivity analyses and geometrical considerations of uncertainty are augmented by analyses of experimental data in which videogrammetric angle measurements were taken simultaneously with precision servo accelerometers corrected for dynamics. An analysis of variance (ANOVA) to examine error dependence on angle of attack, sensor used (inertial or optical), and on tunnel state variables such as Mach number is presented. Experimental comparisons with a high-accuracy indexing table are presented. Small roll angles are found to introduce a zero-shift in the measured angles. It is shown experimentally that, provided the proper constraints necessary for a solution are met, a single-camera solution can be comparable to a 2-camera intersection result. The relative immunity of optical techniques to dynamics is illustrated.

### INTRODUCTION

As demand and usage increases for a particular test technique, issues related to the uncertainty of the measurement technique become more important. For instance, it is not uncommon for better accuracy to be desired as a given technique is used more and more. This has certainly been the case for pitch angle measurements in wind tunnels where the desired accuracy has slowly changed through the years down to less than  $0.01^\circ$  for some applications. Possible new uses of the data from the technique may also arise, once the data is available on a nearly routine basis, that may either require better accuracy or the use of the measurement technique in a different mode. Thus not only is the accuracy of a given technique of

fundamental importance, but, in addition, the sensitivity of the technique to variations in setup geometry, etc. are of interest to assess the possible loss in accuracy that might be necessary to accommodate unique requirements. The importance of supplementing uncertainty analyses with experimental error assessments and the use of modern design of experiments methods (MDOE) has been emphasized in reference 1.

Videogrammetric techniques combine photogrammetry, solid-state area-array cameras and image processing to yield rapid spatial measurements. Videogrammetric techniques have been used at a number of NASA facilities, primarily for the measurement of static aeroelastic model deformation<sup>2</sup>. Variations of videogrammetric techniques include single-camera and multiple-camera implementations, depending on the nature of the application<sup>3</sup>. For example, a single-camera, single-view implementation at the Langley National Transonic Facility (NTF) has been used for the last ten customer tests. A typical image used for measurements at the NTF is presented in figure 1. For most of these tests model static aeroelastic data were obtained for nearly every data point acquired throughout the test, resulting in many thousands of data points of static aeroelastic data per test such as the typical example in figure 2. The interest and demand by industry for these aeroelastic measurements has increased dramatically as the technique has been improved without compromising facility productivity. A more complete and thorough uncertainty analysis will improve the value of this deformation data supplied to industry. More recent investigations with videogrammetric techniques include the measurement of aerodynamic loads<sup>4</sup>, developments for use with micro air vehicles (both fixed- and flapping-wing), for ultra-light and inflatable large space structures during and after deployment<sup>5</sup>, and for in-flight aeroelastic measurements. Techniques are also under study for laboratory and wind tunnel dynamic measurements at frequencies up to 1000 Hz.

The second aerodynamic measurement to be considered is pitch angle measurement, which is a fundamental measurement requirement of all wind tunnels. Note

\* Senior Research Scientist, Senior Member

† Research Scientist, Member

‡ Senior Research Scientist, Member

Copyright © 2002 by the American Institute of Aeronautics and Astronautics, Inc. No copyright is asserted in the United States under Title 17, U.S. Code. The U.S. Government has a royalty-free license to exercise all rights under the copyright claimed herein for Governmental purposes. All other rights are reserved by the copyright owner.

that precision servo accelerometers are normally the primary measurement systems for model pitch angle, not videogrammetric techniques. However, a videogrammetric technique may be a viable candidate for certain wind tunnel pitch angle measurements, especially when space internal to the model is limited, the environmental conditions are harsh, or when the angle changes occur in a plane normal to the gravity vector. Relatively rapid advances in solid-state area-array cameras may enable videogrammetric measurement systems to eventually rival or even surpass the accuracy of accelerometers for wind tunnel model pitch angle measurements. In the near term, videogrammetric techniques will serve as a useful complement to accelerometers for the measurement of pitch angle. An uncertainty analysis will be very useful in the design of videogrammetric pitch angle measurement systems for use in wind tunnels. An uncertainty analysis and error assessment will also help in deciding for which wind tunnels it is advantageous to complement or replace existing inertial angle measurement systems.

An uncertainty analysis that is based solely on photogrammetric principles is inadequate to fully describe the measurement process in aerodynamic applications. For instance, wind-off polars are commonly used during wind tunnel tests to calibrate the videogrammetric measurement system in situ using the onboard accelerometer as the reference standard for angle measurements. There is currently no comparable standard method for calibrating for displacement measurements in situ, although some preliminary testing has occurred using model roll angle under wind-off conditions to compute the linear displacement as a function of semispan. Also note that in aerodynamic testing it is often the change in some parameter that is desired, such as the change in the spanwise wing twist distribution due to aerodynamic loading. Since angle measurements are independent of scale changes, the change in wing twist distribution due to aerodynamic loading can be determined with more confidence than the bending at cryogenic facilities where the temperature changes considerably during testing. Special considerations necessary for the single-camera, single-view technique, such as the shift in spanwise location of targets (assumed to be fixed in the single-camera solution) as wing bending occurs are discussed and evaluated. A simple method to largely compensate for this effect is presented.

#### **DATA REDUCTION EQUATIONS**

The collinearity equations (1) are the most fundamental and important data reduction equations in photogrammetry. They express the relationship that the object point, perspective center, and image point lay on

a straight line. In equations (1) below the image coordinates  $x, y$  have been corrected for optical lens distortion which will be discussed a little later. The photogrammetric principal point is represented by  $x_p, y_p$ , the principal distance is represented by  $c$ , and the object space location is represented by  $X, Y, Z$ . The location of the perspective center is represented by  $X_c, Y_c, Z_c$ . The Euler angles  $\omega, \phi, \kappa$  which orient the image plane to the coordinate system of interest about the  $X, Y, Z$  axes respectively, are used to compute the 9 elements of the rotation matrix given by (2).

$$\begin{aligned} x &= x_p - c \left[ \frac{m_{11}(X - X_c) + m_{12}(Y - Y_c) + m_{13}(Z - Z_c)}{m_{31}(X - X_c) + m_{32}(Y - Y_c) + m_{33}(Z - Z_c)} \right] \\ y &= y_p - c \left[ \frac{m_{21}(X - X_c) + m_{22}(Y - Y_c) + m_{23}(Z - Z_c)}{m_{31}(X - X_c) + m_{32}(Y - Y_c) + m_{33}(Z - Z_c)} \right] \end{aligned} \quad (1)$$

$$\begin{aligned} m_{11} &= \cos \phi \cos \kappa \\ m_{12} &= \sin \omega \sin \phi \cos \kappa + \cos \omega \sin \kappa \\ m_{13} &= -\cos \omega \sin \phi \cos \kappa + \sin \omega \sin \kappa \\ m_{21} &= -\cos \phi \sin \kappa \\ m_{22} &= -\sin \omega \sin \phi \sin \kappa + \cos \omega \cos \kappa \\ m_{23} &= \cos \omega \sin \phi \sin \kappa + \sin \omega \cos \kappa \\ m_{31} &= \sin \phi \\ m_{32} &= -\sin \omega \cos \phi \\ m_{33} &= \cos \omega \cos \phi \end{aligned} \quad (2)$$

The image coordinates  $x, y$  have been corrected for optical lens distortion with equations

$$\begin{aligned} x &= x_d - \delta x_r - \delta x_a \\ y &= y_d - \delta y_r - \delta y_a \end{aligned} \quad (3)$$

Where  $x_d, y_d$  are image plane coordinates for the distorted image point. The terms  $\delta x_r, \delta y_r$  are the radial distortion components along the  $x$  and  $y$  axes. The terms  $\delta x_a, \delta y_a$  are likewise the asymmetrical (or decentering) distortion components. The radial components of lens distortion are given by

$$\begin{aligned} r^2 &= (x - x_s)^2 + (y - y_s)^2 \\ \delta r &= K_1 r^3 + K_2 r^5 + K_3 r^7 + \dots \\ \delta x_r &= K_1 (x - x_s) r^2 + K_2 (x - x_s) r^4 + K_3 (x - x_s) r^6 \\ \delta y_r &= K_1 (y - y_s) r^2 + K_2 (y - y_s) r^4 + K_3 (y - y_s) r^6 \end{aligned} \quad (4)$$

Since  $x, y$  in the above distortion correction equations are the undistorted values yet to be found, the distortion

correction requires iteration with  $x_d, y_d$  as start values to determine the final distortion correction iteratively. The asymmetrical (or decentering) terms  $\delta x_w, \delta y_a$  in (3) are given by

$$\begin{aligned}\delta x_a &= P_1(r^2 + 2x^2) + 2P_2x y \\ \delta y_a &= P_2(r^2 + 2y^2) + 2P_1x y\end{aligned}\quad (5)$$

The collinearity equations can be recast in linear form as

$$\begin{aligned}a_1X + a_2Y + a_3Z &= a_1X_c + a_2Y_c + a_3Z_c \\ a_4X + a_5Y + a_6Z &= a_4X_c + a_5Y_c + a_6Z_c\end{aligned}\quad (6)$$

If 2 or more cameras image a single point and  $a_1$  through  $a_6$  (containing coefficients  $x_p, y_p, c, \omega, \phi, \kappa$ ) and  $X_c, Y_c, Z_c$  are known, then the spatial coordinates  $X, Y, Z$  can be determined with linear least squares. If one of the spatial coordinates is known such as  $Y$ , then a single camera image of a point results in 2 equations in 2 unknowns. With  $Y$  known,  $X$  and  $Z$  can be found from

$$\begin{aligned}X &= X_c + \frac{(Y - Y_c)(a_2a_6 - a_5a_3)}{(a_4a_3 - a_1a_6)} \\ Z &= Z_c - \frac{(X - X_c)a_1 + (Y - Y_c)a_2}{a_3}\end{aligned}\quad (7)$$

Where

$$\begin{aligned}a_1 &= (x - x_p)m_{31} + c m_{11} \\ a_2 &= (x - x_p)m_{32} + c m_{12} \\ a_3 &= (x - x_p)m_{33} + c m_{13} \\ a_4 &= (y - y_p)m_{31} + c m_{21} \\ a_5 &= (y - y_p)m_{32} + c m_{22} \\ a_6 &= (y - y_p)m_{33} + c m_{23}\end{aligned}\quad (8)$$

Once the  $X$  and  $Z$  coordinates are computed for a given semispan location, a slope angle is computed in the  $XZ$  plane by either least squares, or directly when there are only 2 targets per semispan as is the usual case at the NTF. This angle, designated as the raw videogrammetric angle  $\theta_{raw}$ , is given at each semispan  $\eta$  by

$$\theta_{raw}(\eta) = \tan^{-1} \frac{\Delta Z_\eta}{\Delta X_\eta}\quad (9)$$

A 3<sup>rd</sup> order polynomial correction (based on the onboard accelerometer used to determine model pitch angle with wind-off or at low Mach number) is then applied to  $\theta_{raw}$  to yield the corrected angle  $\theta$ . The polynomial correction at each semispan station is given by

$$\theta = b_0 + b_1\theta_{raw} + b_2\theta_{raw}^2 + b_3\theta_{raw}^3\quad (10)$$

The  $b_0$  term serves to zero the angle at 0° pitch angle. The other terms  $b_1$  through  $b_2$  correct for any (normally small) scale differences and nonlinearity when compared to the onboard accelerometer used for pitch angle measurements. These correction coefficients are determined for each run series to partially account for slight instrumentation and/or facility bias changes with time. A pair of reference runs, one before the run set and one after, are made with wind off or, in the case of the NTF, at low mach number such as  $M = 0.1$ . Polynomial correction coefficients are determined for each semispan station over the range of expected pitch angles. The change in twist  $\Delta\theta$  is computed as the difference in  $\theta$  between wind-off and wind-on or

$$\Delta\theta = \theta_{on} - \theta_{off} - \Delta\theta_{(\eta \sim 0)}\quad (11)$$

where  $\theta_{off}$  is taken to be the model pitch angle without flow angularity. The term  $\Delta\theta_{(\eta \sim 0)}$  in (11) is the apparent or real difference between the body local angle measured with videogrammetry and the accepted pitch angle. The angle  $\theta_{off}$  has an additional correction applied at the NTF to account for reference runs being made with flow at low Mach number. This additional correction is based upon the nearly linear relationship between the change in wing twist and the lift coefficient  $c_l$  and the dynamic pressure normalized by the modulus of elasticity, or  $q/e$ . These additional corrections are a function of semispan location. Load coefficients are initially estimated from best guesses of the wing twist versus dynamic pressure. After wing twist data have been acquired and analyzed during the early part of a given test, the load correction coefficients are updated and the previous data re-reduced. The load sensitivity coefficients at each semispan are given by

$$D_\eta = \frac{\Delta\theta_\eta}{\frac{q}{e} c_l}\quad (12)$$

Thus the additional correction  $\delta\theta_\eta$  from reference runs at the NTF is given by

$$\delta\theta_\eta = D_\eta \frac{q}{e} c_l \quad (13)$$

### **SENSITIVITY ANALYSIS**

In order to obtain  $(X,Y,Z)$  from the image coordinates  $(x,y)$ , one can use the single-camera approach in which the collinearity equations are solved for  $(X,Y,Z)$  under a constraint of fixed spanwise location ( $Y = Const.$ ). The single-camera approach is simple, but particularly useful for wind tunnel testing where optical access is very restricted. The more general two-camera or multi-camera approach simultaneously acquires images and the spatial coordinates  $(X,Y,Z)$  are determined from two sets of the image coordinates  $(x,y)$ . The total uncertainty of metric measurements of  $(X,Y,Z)$  is described by the error propagation equation. For simplicity of expression, we replaced  $(X,Y,Z)$  by  $(X_1, X_2, X_3)$  in (14). The total uncertainty in the coordinate  $X_i$  is given by

$$\frac{\text{var}(X_k)}{X_k^2} = \sum_{i,j=1}^M S_{ki} S_{kj} \rho_{ij} \frac{[\text{var}(\zeta_i) \text{var}(\zeta_j)]^{1/2}}{\zeta_i \zeta_j} \quad (14)$$

where  $\rho_{ij} = \text{cov}(\zeta_i, \zeta_j) / [\text{var}(\zeta_i) \text{var}(\zeta_j)]^{1/2}$  is the correlation coefficient between the variables  $\zeta_i$  and  $\zeta_j$ ,  $\text{var}(\zeta_i) = \langle \Delta\zeta_i^2 \rangle$  and  $\text{cov}(\zeta_i, \zeta_j) = \langle \Delta\zeta_i \Delta\zeta_j \rangle$  are the variance and covariance, respectively, and the notation  $\langle \rangle$  denotes the statistical assemble average. Here the variables  $\{\zeta_i, i=1 \dots M\}$  denote a set of the parameters  $(\omega, \phi, \kappa, X_c, Y_c, Z_c)$ ,  $(c, x_p, y_p)$ ,  $(K_1, K_2, P_1, P_2)$ , and  $(x, y)$ . The sensitivity coefficients  $S_{ki}$  are defined  $S_{ki} = (\zeta_i / X_k) (\partial X_k / \partial \zeta_i)$ . Typically the sensitivity analysis of  $(X_1, X_2, X_3)$  to these parameters is made for both the single-camera solution and two-camera solution under the assumption that the cross-correlation is zero.

In wind tunnel testing, the local angle-of-attack (AoA) is usually measured to determine the attitude of a model and wing twist. In a right-hand tunnel coordinate system where  $X$  is in the freestream direction,  $Y$  is in the spanwise direction and  $Z$  is in the upward direction, using two targets placed along the freestream direction on the model, the local angle-of-attack is given by

$$\theta = \tan^{-1} \left( \frac{Z_{(2)} - Z_{(1)}}{X_{(2)} - X_{(1)}} \right) = \tan^{-1} \left( \frac{\Delta Z}{\Delta X} \right) \quad (15)$$

For more targets, a least-squares method is used to calculate the local AoA. The variance of the AoA  $\theta$  is given by

$$\frac{\text{var}(\theta)}{\theta^2} = S_{\theta 1}^2 \frac{\text{var}(Z_{(1)})}{Z_{(1)}^2} + S_{\theta 2}^2 \frac{\text{var}(Z_{(2)})}{Z_{(2)}^2} + S_{\theta 3}^2 \frac{\text{var}(X_{(1)})}{X_{(1)}^2} + S_{\theta 4}^2 \frac{\text{var}(X_{(2)})}{X_{(2)}^2} \quad (16)$$

where the sensitivity coefficients are

$$S_{\theta 1} = \frac{Z_1}{\theta} \frac{1}{1 + (\Delta Z / \Delta X)^2} \frac{1}{X_2 - X_1} \quad (17)$$

$$S_{\theta 2} = -\frac{Z_2}{\theta} \frac{1}{1 + (\Delta Z / \Delta X)^2} \frac{1}{X_2 - X_1} \quad (18)$$

$$S_{\theta 3} = \frac{X_1}{\theta} \frac{1}{1 + (\Delta Z / \Delta X)^2} \frac{Z_2 - Z_1}{(X_2 - X_1)^2} \quad (19)$$

$$S_{\theta 4} = -\frac{X_2}{\theta} \frac{1}{1 + (\Delta Z / \Delta X)^2} \frac{Z_2 - Z_1}{(X_2 - X_1)^2} \quad (20)$$

In order to illustrate the sensitivity analysis, we consider a single-camera system in NTF, where the camera parameters are  $(\omega, \phi, \kappa, X_c, Y_c, Z_c) = (61.6^\circ, 0.2^\circ, -90.8^\circ, 0.1 \text{ in}, -55.2 \text{ in}, 34.5 \text{ in})$ ,  $(c, x_p, y_p) = (26.3 \text{ mm}, -0.23 \text{ mm}, 0.33 \text{ mm})$  and  $(K_1, K_2, P_1, P_2) = (5.96 \times 10^{-4}, 4.17 \times 10^{-5}, -3.72 \times 10^{-4}, 4.98 \times 10^{-4})$ , and the pixel spacing ratio is  $S_h / S_v = 0.422$ . For measurement of the local AoA, two targets are placed along the same spanwise location on a wing at  $(X, Y, Z) = (1, 20, 5)$  inches and  $(X, Y, Z) = (2, 20, 4.5)$  inches. For given errors  $(dx, dy) = (0.05, 0.05)$  pixels in the measurement of the target centroids, we estimate the total uncertainty  $d\theta$  in the local AoA in several situations. Figure 3 shows a schematic of the wind tunnel coordinate system and the position of a camera. As shown in figure 5, when the camera moves up along the  $Z$ -direction while the camera principal distance  $c$  remains invariant, the angular uncertainty  $d\theta$  increases with  $Z_c$  since not only the distance of the camera from the targets increases, but also the angle  $\omega$  decreases. When the camera moves from the position 1 to position 2, the camera principal distance  $c$  can be adjusted to keep the linear distance between the two targets invariant. In this case, the camera principal distance  $c_2$  at the position 2 is given by  $c_2 = c_1 R_2 / R_1$ , where  $c_1$  is camera principal distance at the position 1, and  $R_1$  and  $R_2$  are the distances between the targets and the

camera at the positions 1 and 2, respectively. As shown in figure 5, the angular uncertainty  $d\theta$  is reduced by compensating the camera principal distance at different positions. Another case of interest is when the camera moves along the  $X$ -direction. Figure 6 shows the angular uncertainty  $d\theta$  as a function of  $X_c$  with and without compensation of the camera principal distance  $c$ . Figure 7 shows the angular uncertainty  $d\theta$  as a function of  $\omega$  as the camera moves around the model. Figures 8-11 show the angular uncertainty  $d\theta$  as a function of  $\phi$ ,  $\kappa$ ,  $x_p$ , and  $K_1$ . In the single-camera solution, it is assumed that the spanwise location  $Y$  of the targets is a given constant. However, in actual measurements, the given spanwise location  $Y$  of the targets may not be accurate. When there is an error in the given location  $Y$ , errors occur in  $X$  and  $Z$ . The angular uncertainty  $d\theta$  is plotted in figure 12 as a function of  $dY$  for different values of  $\omega$ . Note that the angular error caused by  $dY$  can be partly thought of as a bias error that is largely reduced by zeroing. In addition a systematic error that is produced by  $dY$  and that varies as a function of the angle can be lessened considerably by the use of reference polars to calibrate the videogrammetric system in terms of known angles.

#### REFERENCE POLAR ANALYSIS

Reference polars are made periodically to calibrate the videogrammetric measurement system in terms of the onboard accelerometer used for precision pitch angle measurements. The change in zero-shift as a function of run set number for a recent test at the National Transonic Facility is plotted in figures 13 and 14. This data represents calibration data for over 3500 data points over a 2.5-month interval. The data is plotted for each of the 6 semispan stations where deformation data were acquired. The inboard station at  $\eta = -0.05$  was used to remove angular sting bending and any bias error common to all semispan stations. The relatively large change in zero-shift evident at  $\eta = 0.77$  and  $0.92$  occurred due to a part change with corresponding new targets at different local angles. Two targets were present at each semispan station  $\eta$ . Target spacing varies from 6 inches at  $\eta = -0.05$  to less than 2 inches at  $\eta = 0.99$ . Although the change in zero-shift inboard is less than  $0.1^\circ$  throughout the 2.5 month test, changes in zero-shift near the tip approached 1 degree. Similar plots for the 1<sup>st</sup>, 2<sup>nd</sup>, and 3<sup>rd</sup>-order terms are given in figures 15 to 20. For those plots the correction computed at an  $\alpha$  of  $6^\circ$  is shown. The changes in zero-shift at the various  $\eta$  stations are plotted versus total temperature  $T_t$  and total pressure  $P_t$  in figures 21 to 24. There appear to be no dramatic correlations with temperature or pressure. Thermal expansion and contraction of the test section that may lead to a non-

repeatable orientation in pitch of the video CCD camera may not necessarily be the cause of the zero-shift since that type of orientation change should be observed at all semispan stations (especially for  $\eta = -0.05$  and  $\eta = 0.35$ ) which is not reflected in the data plots. The values of zero-shift and slope change of the videogrammetric calibration data should be compared to precision servo-accelerometers, which typically have a zero-shift of less than  $0.01^\circ$  and a slope change (at  $\alpha = 6^\circ$ ) of  $0.001^\circ$  or less over several months<sup>14</sup>.

#### ARC LENGTH EFFECT

Wing bending causes the  $Y$  coordinate of wing targets to decrease which causes a bias error in the computation of  $X$  and  $Z$  if not properly accounted for. Consider the case for simple beam bending given by

$$\Delta Z = c_1 Y^2 + c_2 Y^3 \quad (21)$$

If we approximate wing bending by (21), an arc length computation can be used to estimate the amount of shift as a function of  $Y$ . Denoting the variable of integration by  $t^*$ , the arc length  $s(t)$  is given by<sup>6</sup>

$$s(t) = \int_0^t \sqrt{\dot{r}\dot{r}} dt^* \quad (22)$$

where 
$$\dot{r} = \frac{dr}{dt^*} \quad (23)$$

With unit vectors  $\hat{i}$  and  $\hat{j}$  in the  $Y$  and  $Z$  directions respectively, the vector  $\vec{r}$  can be written

$$\vec{r} = t\hat{i} + (c_1 t^2 + c_2 t^3)\hat{j} \quad (24)$$

so that

$$\dot{r} = \hat{i} + (2c_1 t + 3c_2 t^2)\hat{j} \quad (25)$$

For small deflections the integrand in (22) can then be approximated making use of the binomial formula for the result for  $\sqrt{\dot{r}\dot{r}}$  to yield

$$s(t) \approx \int_0^t (1 + 2c_1^2 t^2 + 3c_1 c_2 t^3 + \frac{9}{2} c_2^2 t^4) dt^* \quad (26)$$

which can be evaluated to become

$$s(t) \approx t + \frac{2}{3}c_1^2t^3 + \frac{3}{4}c_1c_2t^4 + \frac{9}{10}c_2^2t^5 \quad (27)$$

Replacing  $t$  with  $(Y - Y_o)$ , where  $Y_o$  is the semispan value at which deflection starts, and with the additional approximation that the change in distance along the curved arc approximates the decrease in  $Y$  of a point on the wing during bending, the following expression is developed for  $\Delta Y$  when  $Y > Y_o$

$$\Delta Y \approx \frac{2}{3}c_1^2(Y - Y_o)^3 + \frac{3}{4}c_1c_2(Y - Y_o)^4 + \frac{9}{10}c_2^2(Y - Y_o)^5 \quad (28)$$

For many cases the 2<sup>nd</sup> order term in (21) alone is sufficient to adequately represent the bending. For those cases the following simplification of (28) is useful for estimating the effect of wing bending on the correct value of  $Y$  needed for the single-camera solution.

$$\Delta Y \approx \frac{2}{3}c_1^2(Y - Y_o)^3 \quad (29)$$

For example, if  $(Y - Y_o) = 30$  inches at  $\eta = 1$  with a tip deflection of 1 inch, then  $\Delta Y \approx 0.022$  inch. In other words the correct  $Y$  to use for the deflected tip target should be less by this  $\Delta Y$ . A partial correction for this effect can be implemented by first calculating the  $X, Z$  coordinates without correction for  $\Delta Y$ , then determine a first estimate of  $c_1$  for use in (29) to get an estimate of the correction  $\Delta Y$  to apply before recomputing  $X, Z$  with the single-camera solution. One or two iterations should be sufficient for typical applications.

## **PITCH ANGLE ACCURACY ASSESSMENT**

### **16-Ft Transonic Tunnel Entry**

To measure pitch angle in a wind tunnel, precision servo accelerometers are currently the primary measurement system rather than videogrammetric techniques. However, videogrammetric techniques can be attractive when space internal to the model is limited, the environmental conditions are harsh, or when the angle changes occur in a plane normal to the gravity vector. Even under the wide range of normal operating conditions in which inertial angle measurement methods are well suited for the measurement of pitch angle, videogrammetric techniques can often serve as a useful complement to accelerometers.

As part of a broader effort to develop and validate an advanced dynamics-compensation capability for the inertial angle sensing measurements that are routinely made in wind tunnel tests at NASA Langley Research

Center, videogrammetric and inertial angle sensors were compared under identical circumstances<sup>7</sup>. These comparisons were conducted in the Langley 16-Ft Transonic Tunnel on a high-speed research (HSR) vehicle. Comparisons were made with wind off and with wind on. Two independent servo accelerometers were mounted internal to the model in the usual way, and two single-camera videogrammetric pitch-sensing systems were also used. The two videogrammetric systems were mounted on separate tripods (figure 25), but viewed the same 5 targets on the model (figure 26). During wind-off measurements, an external high-precision inclinometer system<sup>8</sup> was used as a reference for comparison of both onboard inertial systems and both videogrammetric systems. The reference system's angle measurement was subtracted from the measured value of pitch angle at the same set point for each of the four angle transducers under comparative evaluation, with the residual described as the "error" in the corresponding transducer.

A wind-off run consisted of measurements from nominal set-point angles of  $-4^\circ$  to  $+10^\circ$  in  $2^\circ$  steps, with  $0^\circ$  replicated at the end. Three such wind-off runs were executed. The first was a pre-test run, before any wind-on measurements had been made. The second, denoted as the "mid-test" run, occurred the next day, after wind-on operations had begun. A post-test run was also executed after all wind-on operations had been completed, six days after the pre-test run. This period included a weekend in which there were no tunnel operations. (Note that this tunnel entry was used to support multiple objectives and the pitch instrument measurements were made only during a part of the total entry.)

Sixteen wind-on runs were executed in addition to the wind-off runs. Quality assurance tactics (blocking and randomization) drawn from the Modern Design of Experiments (MDOE) were used to minimize unexplained variance. For example, the sixteen wind-on runs were grouped by time into four blocks, within each of which four Mach numbers – 0, 0.3, 0.8, and 0.9 – were set in a different random order. The four runs at Mach 0 were obviously wind-off runs but were analyzed with the wind-on data because these runs were interspersed among other runs with flow, and because an external precision inclinometer was not used as a reference in these wind-off runs, as was the case in the three wind-off runs analyzed separately.

The outputs of the two accelerometers were each electronically corrected for dynamic effects described as "stingwhip", a phenomenon in which angular acceleration of a vibrating sting adversely influences the quality of pitch measurements made with an

accelerometer<sup>9</sup>. One of the two stingwhip-corrected accelerometer outputs was used as a reference upon which to base differential pitch measurements made with all the other instruments under study. This eliminated angle of attack set point error from the unexplained variance, which permitted much more subtle effects to be resolved with the correspondingly lower noise level. This choice of a reference was based on the fact that precision servo accelerometers represent the current state of the art in wind tunnel pitch angle measurements.

The Mach number set-point order was randomized within each block to increase the degree of statistical independence in the data and thereby defend against the effects of systematic variations due to such factors as drift in the instrumentation and data systems, changes over time in flow angularity and wall-effects, and various effects attributable to systematic temperature variations, etc.<sup>10-12</sup>. At each Mach number, nominal set-point angles of  $-4^\circ$  to  $+10^\circ$  in  $2^\circ$  steps were acquired in random order to further defend against the effects of any systematic variations that might have been in play while data were acquired at a given Mach number. Figure 27 displays the temperature time history over the time the sixteen wind-on runs were acquired. This figure illustrates systematic changes in tunnel temperature over periods of time in which individual (randomized) polars were acquired, and even wider systematic temperature variations from Mach number to Mach number. The randomization is intended to decouple Mach and pitch angle effects from any systematic error that could be induced by such temperature variations, or other systematic error effects.

**Analysis of Variance** Tables I and II present the results of an analysis of variance (ANOVA) conducted on the wind-off and wind-on data, respectively. The variables A, B, and C in the wind-off ANOVA represent angle of attack, run – a surrogate for elapsed time (pre-test, mid-test, or post-test), and instrument, respectively. The B and C variables were treated as categorical (discrete-level) variables (three runs and four instruments – the two servo accelerometers and two videogrammetric systems) while angle of attack was treated as numeric (continuous), and modeled to first order. Therefore the “A” variable in Table I represents the slope of pitch error regressed against angle of attack set point.

For the wind-on ANOVA table, A and C are again angle of attack and instrument, respectively, but the B variable now represents Mach number. Angle of attack was treated as numeric. The high precision afforded by MDOE blocking techniques that minimized set-point error and systematic variations permitted terms in a wind-on angle of attack model as high as 4<sup>th</sup>-order to be

resolved in the presence of the remaining unexplained variance. See Table II. The wind-on B and C variables were treated as categorical variables. There were four discrete Mach numbers (0, 0.3, 0.8, and 0.9) and six pitch instruments. In addition to the two servo accelerometers and two videogrammetric systems used in the wind-off ANOVA, the wind-on ANOVA added pitch estimated from the arc sector corrected for sting bending, and the stingwhip-corrected output of the servo accelerometer not being used as a reference for the differential wind-on pitch measurements.

The wind-off ANOVA in Table I reveals statistically significant main effects for angle of attack, elapsed time, and instrument, as well as a significant interaction between elapsed time and instrument. The “F-value” is relatively high for each of these factors. This represents the portion of explained variance attributable to a given source, normalized by the unexplained variance. The “prob > F” column of the ANOVA table indicates the probability that an F-value this large could occur from ordinary chance variations in the data. Small values imply that it is unlikely that the effect could appear so great by chance alone, and that therefore there is a high probability that the effect is not due to chance but is in

**Table I: Wind-off ANOVA**

Source	Sum of Squares	DF	Mean Square	F Value	Prob > F
<b>Model</b>	0.009039	17	0.000532	38.7	< 0.0001
A	6.54E-05	1	6.54E-05	4.8	0.0317
B	0.004477	2	0.002239	163.0	< 0.0001
C	0.002826	3	0.000942	68.6	< 0.0001
AB	1.01E-05	2	5.06E-06	0.4	0.6929
AC	5.79E-05	3	1.93E-05	1.4	0.2469
BC	0.001603	6	0.000267	19.4	< 0.0001
<b>Residual</b>	0.001236	90	1.37E-05		
LOF	0.00119	78	1.53E-05	3.9	0.0059
PE	4.66E-05	12	3.89E-06		
<b>Cor Total</b>	0.010276	107			

fact real. If “prob > F” is less than 0.05, for example, then we can say with at least 95% confidence that the associated effect is real, and not an artifact of experimental error in the data. Note that “prob > F” is very small for the A, B, and C main effects in the wind-off data, and for the BC two-way interaction.

The ANOVA table can indicate roughly the relative size of the explained (significant) effects. Note, for example, that the largest F-value in the wind-off data occurs for variable B, which is run number. This implies that averaged across all instruments and all angles of attack in the experiment, the pitch error

changes over time. That is, the wind-off ANOVA table indicates that the pitch error should not be expected to

**Table II: Wind-on ANOVA**

Source	Sum of		Mean	F	
	Squares	DF	Square	Value	Prob > F
<b>Block</b>	0.0009	3	0.0003		
<b>Model</b>	1.1439	81	0.0141	256.5	< 0.0001
A	0.0232	1	0.0232	421.5	< 0.0001
B	0.2876	3	0.0959	1741.0	< 0.0001
C	0.3548	5	0.0710	1288.8	< 0.0001
A2	0.0034	1	0.0034	61.8	< 0.0001
AB	0.0383	3	0.0128	231.9	< 0.0001
AC	0.0667	5	0.0133	242.3	< 0.0001
BC	0.2577	15	0.0172	312.0	< 0.0001
A3	0.0006	1	0.0006	10.2	0.0015
A2B	0.0071	3	0.0024	42.8	< 0.0001
A2C	0.0080	5	0.0016	29.2	< 0.0001
ABC	0.0789	15	0.0053	95.5	< 0.0001
A4	0.0005	1	0.0005	10.0	0.0017
A3B	0.0004	3	0.0001	2.2	0.0904
A3C	0.0009	5	0.0002	3.1	0.0084
A2BC	0.0159	15	0.0011	19.3	< 0.0001
<b>Residual</b>	0.0376	683	0.0001		
<b>CorTot</b>	1.1825	767			

be the same in the pre-test, mid-test, and post-test runs. Figure 28 shows this effect clearly. The “I-beam” symbols in this figure and others represent “least significant difference” (LSD) intervals, which indicates how much difference there must be in two responses before they can be resolved with a specified level of confidence – 95% in this case. Note in figure 28 that the LSD intervals overlapped for the pre-test runs but that by the mid-test run (acquired the next day after the pre-test run), a difference between the video and the accelerometer errors could be resolved with at least 95% confidence. Note also that the two video systems and the two accelerometer systems could not be resolved from each other. By the time the wind-off post-test run was acquired, five days after the mid-test run, differences between the two like instruments were beginning to appear. The two video systems could not quite be resolved with 95% confidence but a difference in the two accelerometers was clearly evident.

The wind-off ANOVA table indicates a significant BC interaction (F-value greater than 19 and corresponding “prob > F” of less than 0.0001). This simply means that the change in pitch-angle error with time depends on the instrument. Again, figure 28 illustrates what this means graphically. The error in the videogrammetric instruments peaked in the mid-test run but by the end of

the test had returned to nominally the same level as the pre-test run. The accelerometers, on the other hand, were relatively stable from the pre-test to the mid-test run, but degraded somewhat by the end of the six-day test.

Note that these effects are only relative. In absolute terms, the wind-off pitch error was largely within the  $\pm 0.01^\circ$  tolerances generally specified for high-precision wind tunnel testing. However, the clear tendency revealed in this analysis for instrument performance to change with time, and in a way that differs from one instrument to another, provides some justification for experimental tactics such as randomization and blocking (utilized in the wind-on portion of the test) that are designed to decouple independent variable effects from these time-varying systematic errors.

Figures 29 and 30 show how the wind-off pitch error varied with angle of attack during the pre-test (black), mid-test (red), and post-test (green) runs for the inertial and videogrammetric systems. The magnitude of the change in error (apparent instrument drift) across the total elapsed time of the test was comparable for both classes of instrument. These figures also show the mild dependence of pitch error on angle of attack set point, as evidenced by the slight slope of the first-order fits of error to angle of attack. The fact that this angle of attack dependence is so mild is reflected in the wind-off ANOVA Table by the fact that the F-value for factor A – slope of angle of attack fit – is the smallest of the statistically significant wind-off effects. (The AB and AC interaction effects have smaller F-values, but the corresponding “prob > F” values are too high to attribute these F values to anything other than random variations in the data. This implies that there is no detectable interaction between the slope of the fit of pitch error against angle of attack, and either time or instrument.) This is confirmed in figures 29 and 30 by the fact that all the plotted lines are generally parallel. Note also that notwithstanding the non-zero slope of pitch error against angle of attack set point, the change in pitch error (drift) was generally within the  $0.01^\circ$  across the entire angle of attack range tested ( $-4^\circ$  to  $+10^\circ$ ).

The wind-on analysis of variance in Table II showed statistically significant main effects for all three independent variables and for all three of their two-way interactions. The three-way interaction involving all of these variables was significant as well, as were the interactions of the B, C, and BC terms with the linear and curvature terms in the angle of attack dependence. Furthermore, the B and C variables (but not the BC interaction) exhibited a significant interaction with the cubic term of a 4<sup>th</sup>-order fit of change in pitch against

angle of attack. Finally, there was a significant quartic angle of attack term that did not interact with B, C, or BC.

The significant higher order angle of attack terms in the wind-on data indicates that delta-pitch varied in a complex way with angle-of-attack set point when the wind was on. The fact that these higher-order terms exhibited interactions with the B and C variables (Mach number and instrument) indicate that the complex angle of attack dependence depended on instrument and Mach number. Figures 31, 32, and 33 illustrate this.

Figure 34 reveals the effects of stingwhip on conventional servo-accelerometers, which has motivated interest in the possible application of videogrammetric methods to pitch angle measurements that are not affected as much by stingwhip or other dynamic effects. At low Mach numbers there is little or no detectable stingwhip, but the errors are large at higher Mach numbers compared to the  $0.01^\circ$  level that constitutes the entire angle of attack error budget for precision wind tunnel testing such as performance testing. This explains why Mach number is indicated in the wind-on ANOVA table to be a highly significant factor in determining delta-pitch. The fact that the angle of attack dependence of delta-pitch varies in Figure 34 so dramatically with Mach number further reveals why the ANOVA table indicates large interactions between Mach number and the various-order terms in the AoA dependence.

Figure 35 compares delta-pitch for a variety of instruments at the highest Mach number tested – 0.9. Each instrument displays a different AoA dependence, as forecasted in the ANOVA table by the significant interactions between various AoA coefficients and instrument. These differences manifest themselves according to certain patterns, however. Note that for both of the video systems as well as the stingwhip-corrected inertial system, the variation in delta-pitch is small across all angles of attack between  $-4^\circ$  and  $+10^\circ$ , and relatively small in absolute terms as well. The variations are substantially larger for the uncorrected inertial systems and for the arc-sector corrected for sting bending, both common techniques in current widespread use for pitch-angle measurements. Errors in these latter systems approached a quarter degree – 25 times the error budget for angle of attack in typical precision wind tunnel tests.

**1-CAMERA/2-CAMERA COMPARISON**

Static laboratory tests were conducted to compare angle measurements made with the single camera solution (7) and angle measurements using 2-camera intersection. The 2-camera measurement system used

for these tests was developed for NASA by the High Technology Corporation<sup>13</sup>. The measurement system employs 2 progressive scan cameras with a resolution of 640 X 480. Software includes programs for image acquisition, target tracking, centroid calculation,, camera calibration and 2-camera photogrammetric intersection. The centroid files output from each camera separately were used in an off-line reduction to produce the 2 sets of 1-camera results. A high-accuracy indexing table that has been calibrated to better than 1 arcsecond ( $0.0003^\circ$ ) was used as the standard. The pitch angle was varied over a range of  $-10^\circ$  to  $30^\circ$  in  $1^\circ$  increments. A second indexing table was used to introduce roll angles of  $0^\circ$ ,  $\pm 2^\circ$ , and  $\pm 4^\circ$  to assess the effect of an unknown roll on the angle data. No correction was made for the roll to simulate the case for wind tunnel models where an unknown roll may be present. Small roll angles are seen to introduce a zero-shift in the measured values. The 2-camera intersection results are presented in figure 36. For this figure and the following 2 plots, the known set angle is subtracted, leaving the angular error compared to the known standard. Figures 37 and 38 depict the single-camera results for the same 2 cameras as used to acquire the 2-camera intersection results. The same centroid data (image plane data) were used for the intersection results as for the two 1-camera solutions. Note the similarity of the 2-camera intersection and 1-camera result of camera #1. 1-Camera results for camera #2 are somewhat better than either the results using camera #1 or the results using both cameras. The excellent results found for camera #2 suggest that given the proper experimental situation, comparable or even better angular measurements can be made with a single camera than with 2-camera intersection. Summary results of the mean and standard deviation of the error (compared to the indexing table) are presented in Table III and figure 39.

**Table III: Mean and std dev of error**

	mean	std
2-camera	0.0136°	0.0138°
1-camera #1	0.0146°	0.0101°
1-camera #2	0.0033°	0.0028°

**DYNAMIC EFFECTS**

Both the videogrammetric technique and the commercially available Optotrak™ system have been evaluated to assess their immunity to dynamics as part of a series of tests conducted on the newly developed sting-whip corrected inertial devices<sup>9</sup>. A shaker at constant output level was varied from 0 to 70 Hz in small increments. The plate containing 6 LEDs used by the Optotrak system and 6 passive targets used by the videogrammetric system (figure 40) was excited in

separate tests in both the vertical and the horizontal directions. Data were acquired with both optical systems at each frequency. Data from these dynamic tests are presented in figures 41 and 42. The difference between the mean angle measured with each system is also plotted. The 2 systems agreed within  $\pm 0.002^\circ$  for horizontal excitation and agreed within  $\pm 0.005^\circ$  for vertical excitation. Larger variations of up to  $0.015^\circ$  for both systems during vertical excitation at around 2 Hz are likely due to an actual change of mean angle of the excited mounting plate. Similar excitation can cause errors of up to  $0.25^\circ$  for inertial sensors (at resonant frequencies of the experimental arrangement) if not corrected by special techniques recently implemented for routine use in large wind tunnels<sup>9</sup>.

### **CONCLUDING REMARKS**

Data reduction equations for videogrammetric deformation and pitch angle measurements have been presented. A correction due to reference polars being taken with wind-on has been described. A sensitivity analysis for a number of parameters associated with the photogrammetry process has been presented. The variation of calibration coefficients from reference polars taken at the National Transonic Facility have been discussed. The potential error in the known coordinate for 1-camera photogrammetry has been described and a method to partially correct for this effect presented. Results from a pitch angle accuracy assessment test at the 16-Ft Transonic Tunnel have been discussed. It was shown that videogrammetric techniques can nearly match the quality of sting-whip corrected inertial devices and clearly exceed the quality of non-corrected inertial devices during transonic testing. It was shown that given suitable experimental arrangements that single-camera videogrammetric pitch angle measurements can be comparable to those made with 2-camera intersection. The relative immunity of videogrammetric techniques to dynamics has been demonstrated with a laboratory experiment that includes comparison data from the commercially available Optotrak™ measurement system.

### **ACKNOWLEDGEMENTS**

Tom D. Finley and Bradley L. Crawford, NASA Langley Research Center, are acknowledged for development and application of the stingwhip-corrected inertial measurement devices used as reference for the pitch angle assessment at the 16-Ft Transonic Tunnel. Bradley L. Crawford is also acknowledged for his outstanding experiment design for the 16-Ft test. William K. Goad, Kenneth H. Cate and Harriett R. Dismond and the technical staff of the 16-Ft Transonic Tunnel at NASA Langley are acknowledged for technical support and assistance during testing. Dr. John C. Hoppe of NASA Langley is acknowledged for

the Optotrak data taken in the presence of dynamics that is presented here.

### **REFERENCES**

1. Hemsch, M. J., "Some General Notations in Measurement Uncertainty Analysis", *Ground Testing Technical Committee*, Vol. 3, No. 3, 2002, p 17.
2. Burner, A. W. and Liu, T., "Videogrammetric model deformation measurement technique", *Journal of Aircraft*, Vol. 38, No. 4, 2001, pp. 745-754.
3. Liu, T., Cattafesta, L., Radezsky, R., and Burner, A. W.; "Photogrammetry applied to wind tunnel testing", *AIAA J.* Vol. 38, No. 6, 2000, pp. 964-971.
4. Liu, T., Barrows, D. A., Burner, A. W., and Rhew, R. D.: "Determining Aerodynamic Loads Based on Optical Deformation Measurements", *AIAA J.* Vol. 40, No. 6, 2002, pp. 1105-1112
5. Pappa, R. S., Jones, T. W., Black, J.T., Walford, A., Robson, S., and Shortis, M. R., "Photogrammetry Methodology Development for Gossamer Spacecraft Structures", 43<sup>rd</sup> AIAA/ASME/ASCE/AHS/ASC Structures, Structural Dynamics, and Materials Conference, 3<sup>rd</sup> AIAA Gossamer Spacecraft Forum, Denver, CO, April 2002.
6. Kreyszig, E.: *Advanced Engineering Mathematics*. John Wiley, New York, 1965, chap. 5, pp. 290-291.
7. Crawford, B. L. and Finley T. D., "Results From a Sting Whip Correction Verification Test at the Langley 16-Foot Transonic Wind Tunnel", *40th AIAA Aerospace Sciences Meeting and Exhibit*, Reno, Nevada, AIAA 2002-0879, January 14-17, 2002.
8. Ferris, A. T., "Angle Measurement System (AMS) Operator's Manual", NASA Langley LMS-TD-0615, 1999.
9. Crawford, B. L. and Finley, T. D., "Improved Correction System for Vibration Sensitive Inertial Angle of Attack", *38th AIAA Aerospace Sciences Meeting and Exhibit*, Reno, Nevada, AIAA 2000-0415, January 10-13, 2000.
10. DeLoach, R. "Improved Quality in Aerospace Testing Through the Modern Design of Experiments". AIAA 2000-0825. *38th AIAA Aerospace Sciences Meeting and Exhibit*. Reno, NV. Jan 2000.
11. DeLoach, R., Hill, J. S., and Tomek, W. G. "Practical Applications of Blocking and Randomization in a Test in the National Transonic Facility" (invited)

AIAA 2001-0167. *39th AIAA Aerospace Sciences Meeting and Exhibit*. Reno, NV. Jan 2001.

12. DeLoach, R. "Tactical Defenses Against Systematic Variation in Wind Tunnel Testing" AIAA 2002-0885, *40th AIAA Aerospace Sciences Meeting & Exhibit*. January 14-17, 2002.

13. Liu, T., Radeztsky, R., Garg, S., and Cattafesta, L. "A Videogrammetric Model Deformation System and Its Integration with Pressure Paint", AIAA 99-0568, 1999.

14. Finley, T. D., *Private Communication*, NASA Langley Research Center, June 2002.



Figure 1. Typical image used for videogrammetric model deformation measurements with polished paint targets.

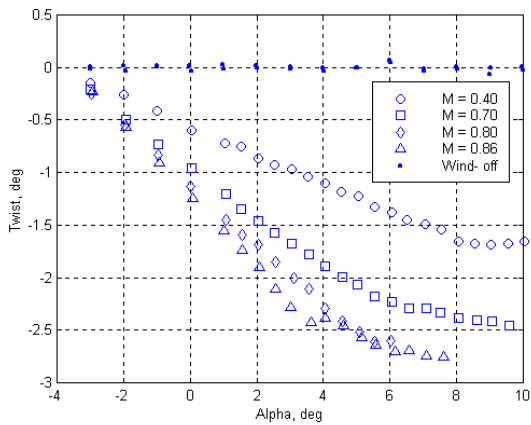


Figure 2. Typical videogrammetric model deformation data.

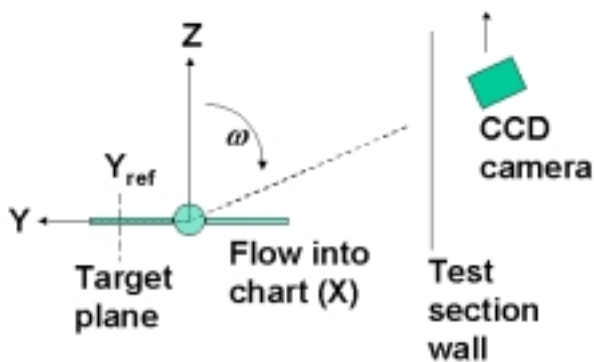


Figure 3. Sketch of coordinate system and motion of camera for first case.

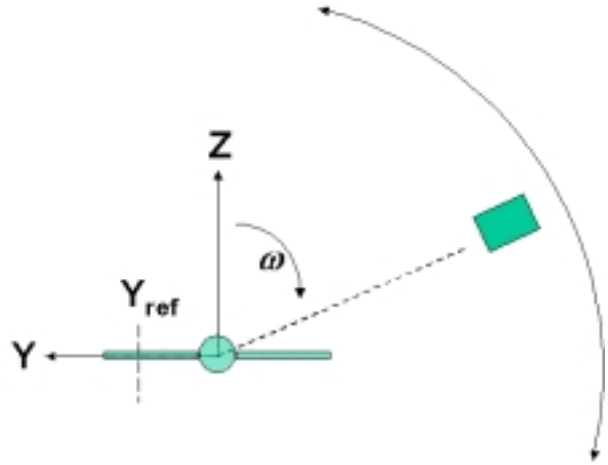


Figure 4. Sketch of coordinate system and rotation of camera with constant  $\omega$

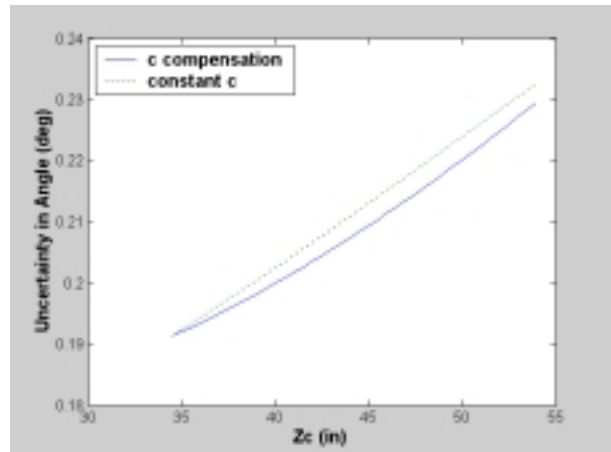


Figure 5. Uncertainty in angle as a function of increasing  $Z_c$  (and corresponding decrease in  $\omega$ ).

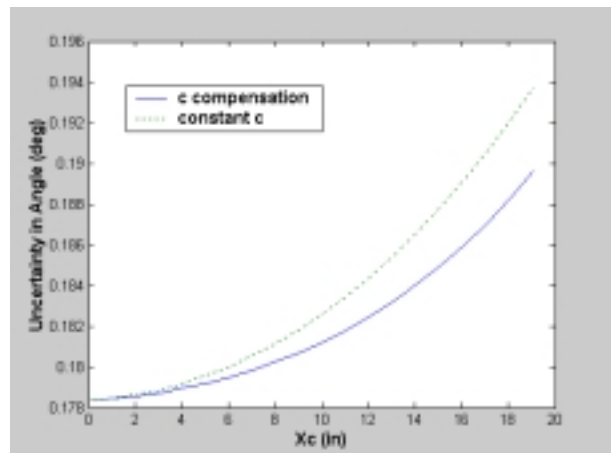


Figure 6. Uncertainty in angle as a function of increasing  $X_c$ .

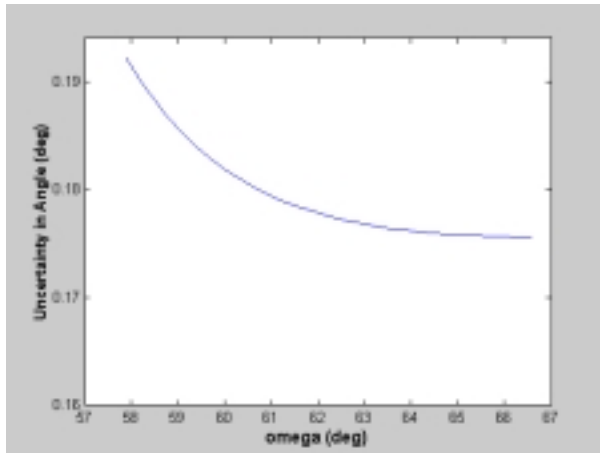


Figure 7. Uncertainty in angle as  $\omega$  is varied.

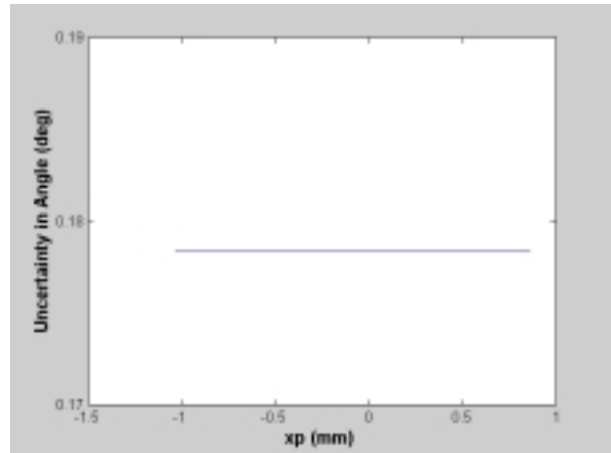


Figure 10. Uncertainty in angle as a function of  $x_p$ .

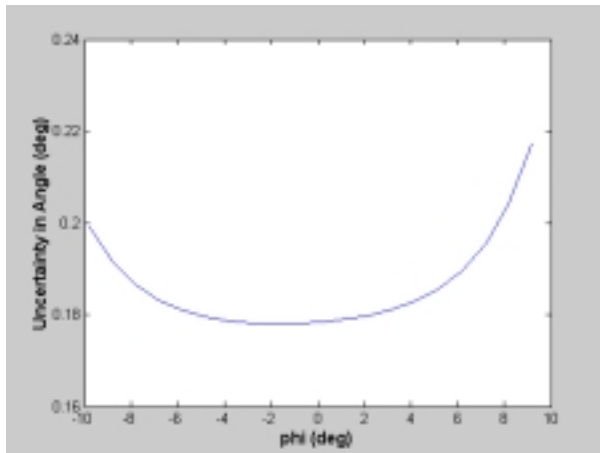


Figure 8. Uncertainty in angle as a function of  $\phi$ .

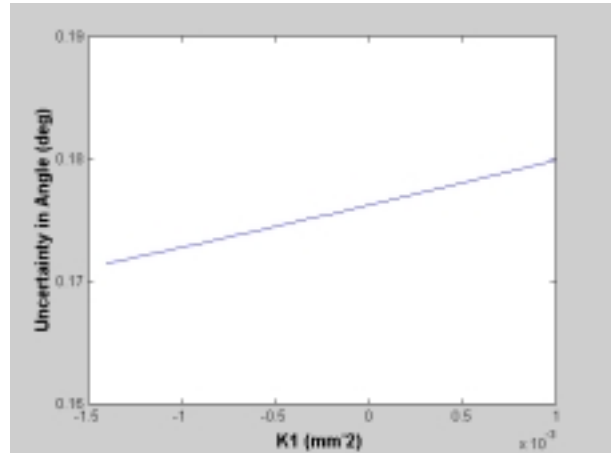


Figure 11. Uncertainty in angle as a function of  $K_1$ .

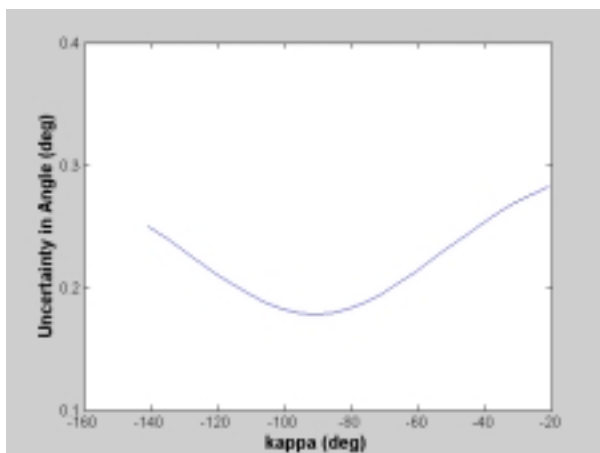


Figure 9. Uncertainty in angle as a function of  $\kappa$ .

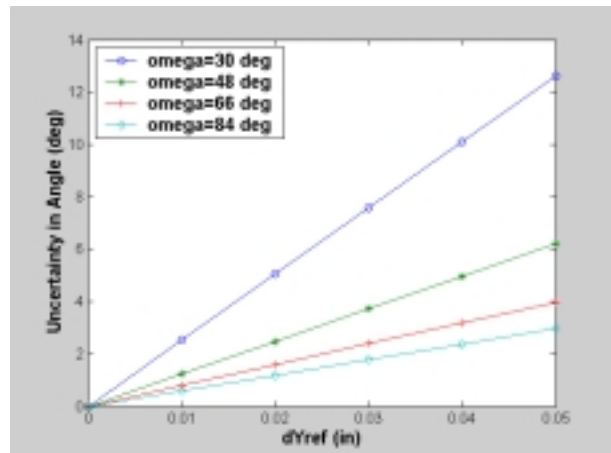


Figure 12. Uncertainty in angle as a function of error in  $Y_{ref}$ .

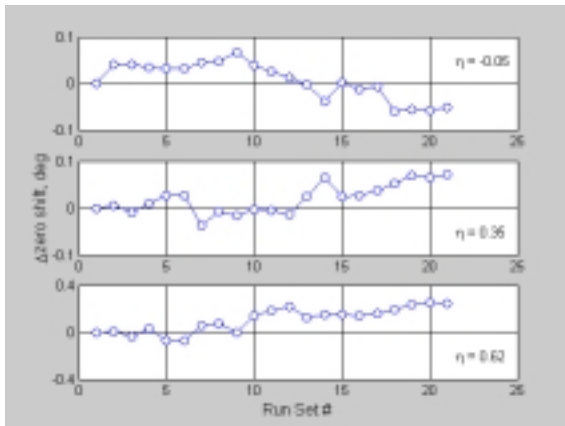


Figure 13. Change in zero-shift as a function of run set number over 2.5 months for inboard semispan stations  $\eta$ .

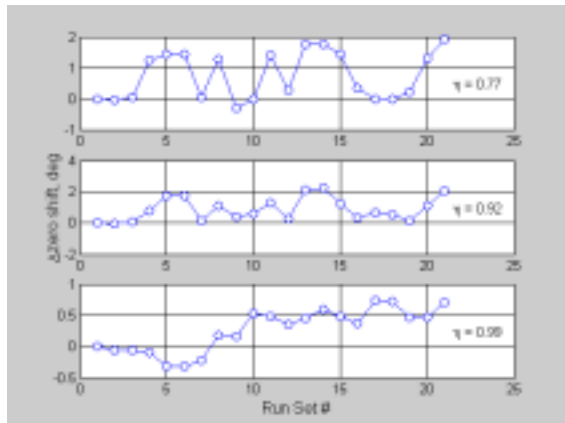


Figure 14. Change in zero-shift as a function of run set number over 2.5 months for outboard semispan stations  $\eta$ .

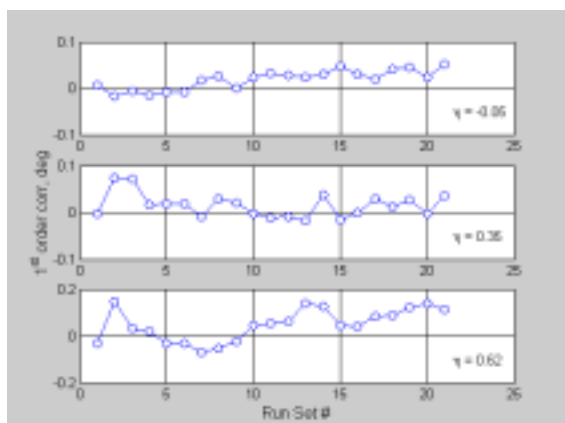


Figure 15. 1<sup>st</sup> order correction at  $\alpha = 6^\circ$  as a function of run set number over 2.5 months for inboard semispan stations  $\eta$ .

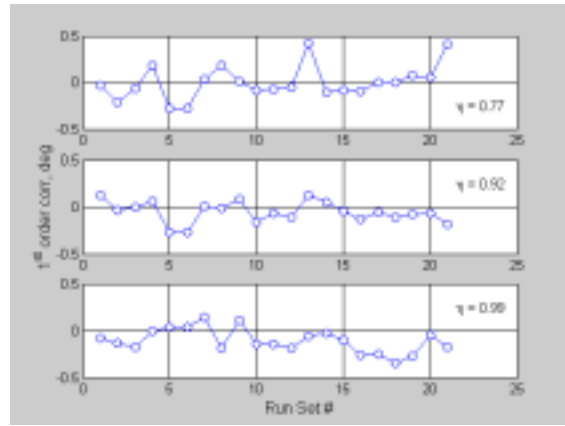


Figure 16. 1<sup>st</sup> order correction at  $\alpha = 6^\circ$  as a function of run set number over 2.5 months for outboard semispan stations  $\eta$ .

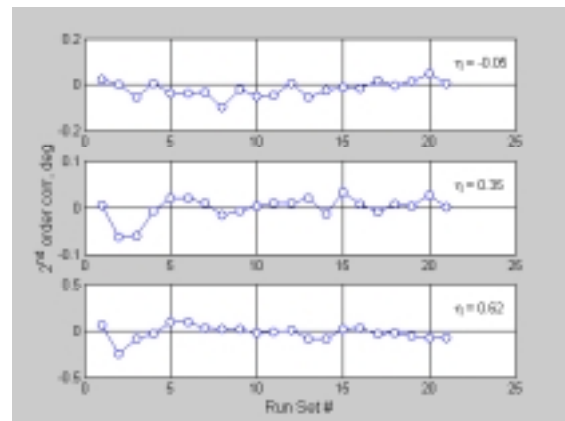


Figure 17. 2<sup>nd</sup> order correction at  $\alpha = 6^\circ$  as a function of run set number over 2.5 months for inboard semispan stations  $\eta$ .

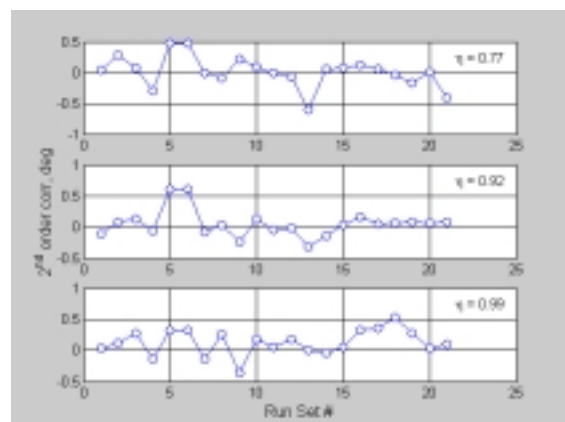


Figure 18. 2<sup>nd</sup> order correction at  $\alpha = 6^\circ$  as a function of run set number over 2.5 months for outboard semispan stations  $\eta$ .

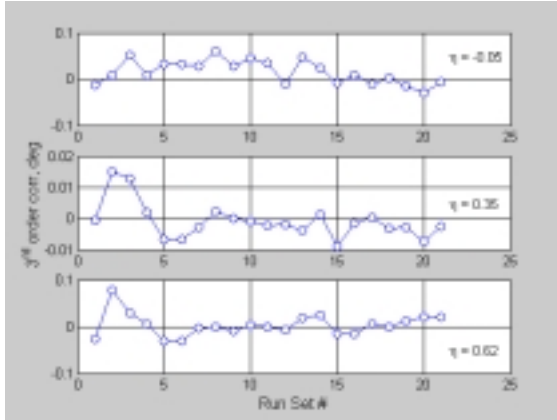


Figure 19. 3<sup>rd</sup> order correction at  $\alpha = 6^\circ$  as a function of run set number over 2.5 months for outboard semispan stations  $\eta$ .

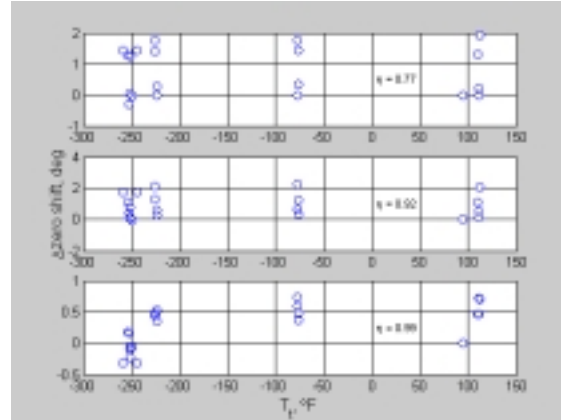


Figure 22.  $\Delta$ zero-shift as a function of  $T_t$  over 2.5 months for outboard semispan stations  $\eta$ .

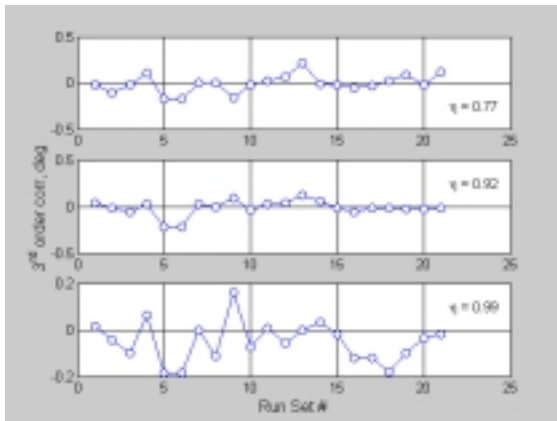


Figure 20. 3<sup>rd</sup> order correction at  $\alpha = 6^\circ$  as a function of run set number over 2.5 months for inboard semispan stations  $\eta$ .

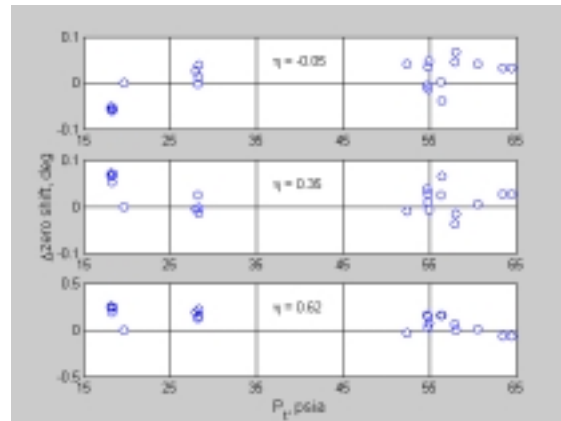


Figure 23.  $\Delta$ zero-shift as a function of  $P_t$  over 2.5 months for inboard semispan stations  $\eta$ .

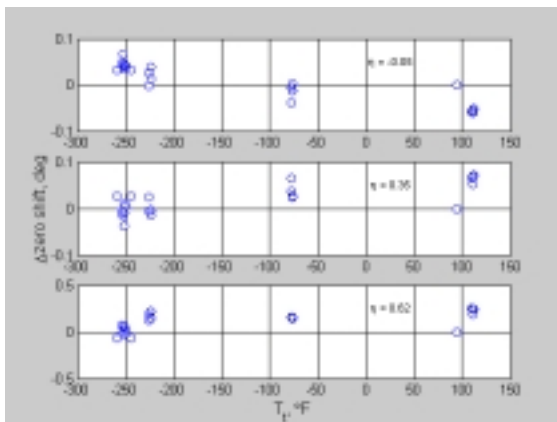


Figure 21.  $\Delta$ zero-shift as a function of  $T_t$  over 2.5 months for inboard semispan stations  $\eta$ .

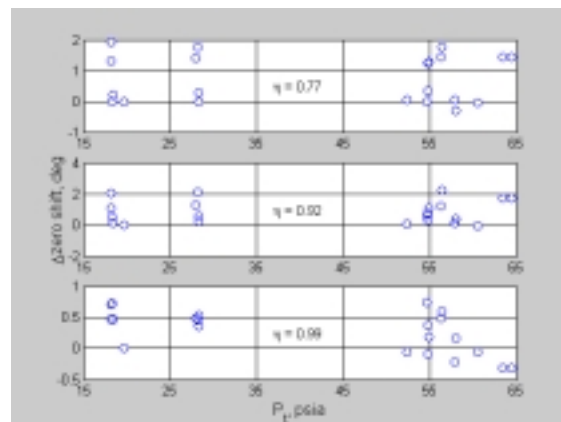


Figure 24.  $\Delta$ zero-shift as a function of  $P_t$  over 2.5 months for outboard semispan stations  $\eta$ .



Figure 25. Two video cameras used for pitch angle evaluation test at 16-Ft Transonic Tunnel.



Figure 26. Model at 16-Ft Transonic Tunnel with optical targets and AMS in place for verification.

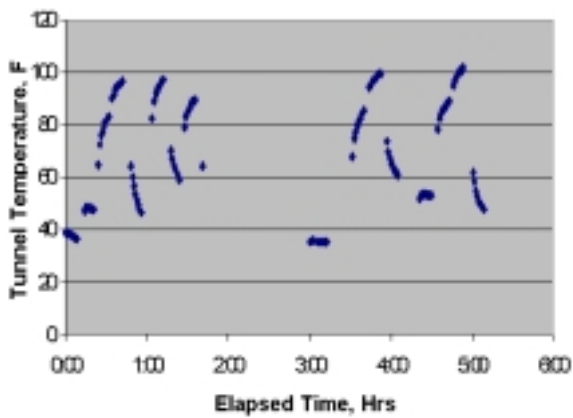


Figure 27. Temperature variations over a 60° F range in fewer than 6 hours can cause systematic variations that are addressed by randomizing and blocking the data.

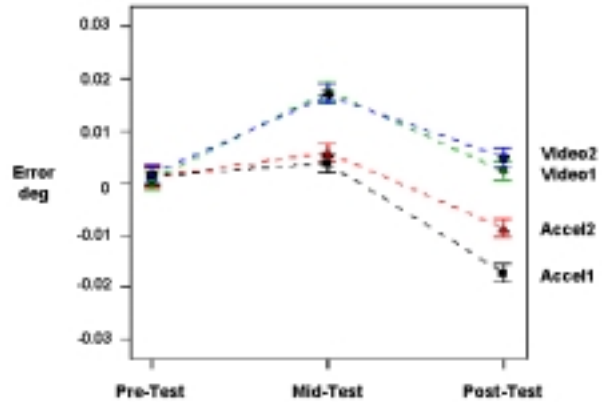


Figure 28. Error compared to AMS as a function of time.

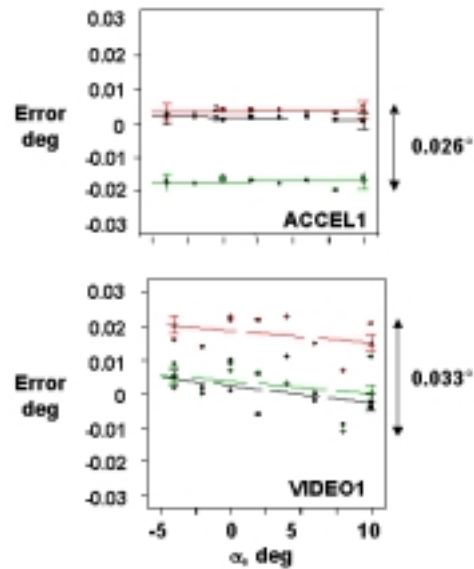


Figure 29. Error compared to AMS for accelerometer #1 and videogrammetric #2, for three elapsed times throughout test.

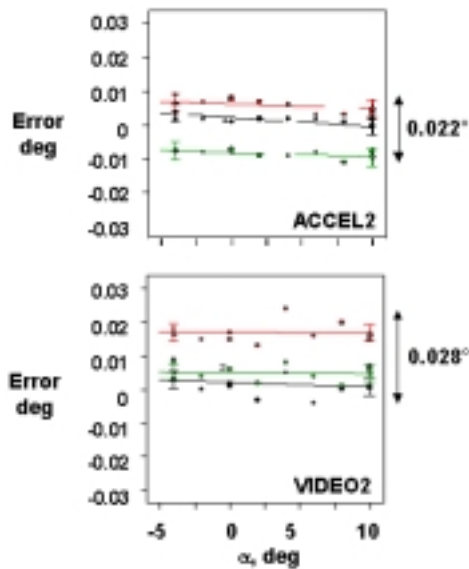


Figure 30. Error compared to AMS for accelerometer #2 and videogrammetric measurement #2, for three elapsed times throughout test.

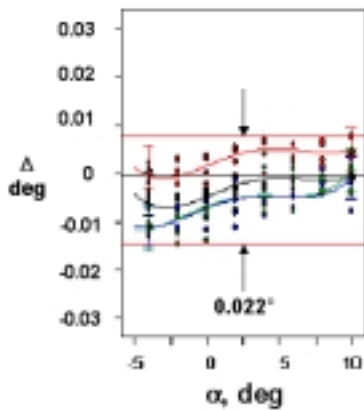


Figure 31. Differences,  $\Delta$ , of the 1st corrected accelerometer measurements using the 2nd corrected accel as reference at  $M = 0.0, 0.3, 0.8, 0.9$ .

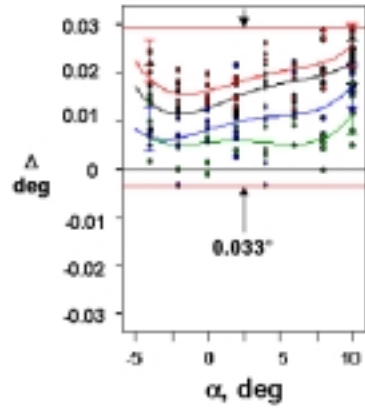


Figure 32. Differences,  $\Delta$ , of the 1st videogrammetric measurements using the 2nd corrected accel as reference at  $M = 0.0, 0.3, 0.8, 0.9$ .

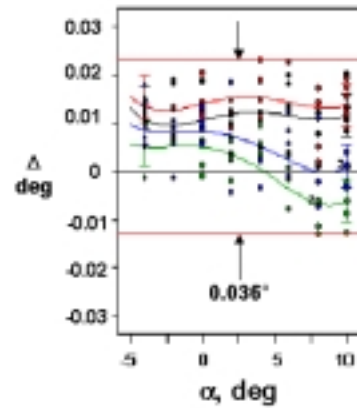


Figure 33. Differences,  $\Delta$ , of the 2nd videogrammetric measurements using the 2nd corrected accel as reference at  $M = 0.0, 0.3, 0.8, 0.9$ .

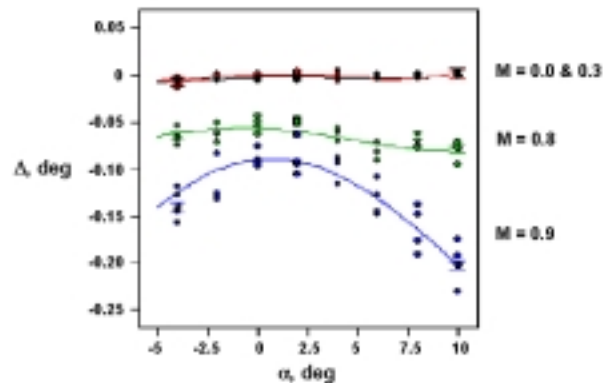


Figure 34. Accelerometer data uncorrected for sting whip dynamics at Mach 0, 0.3, 0.8, and 0.9.

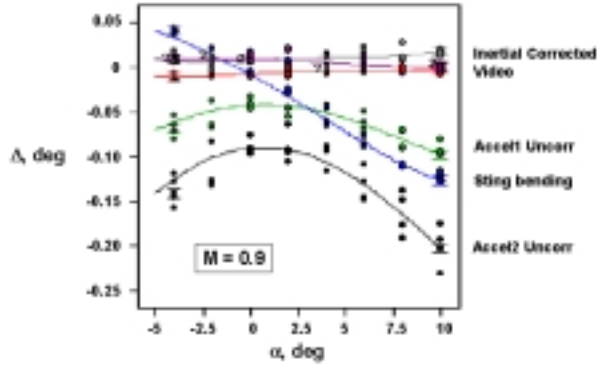


Figure 35. Inertial, videogrammetric, and sting bending differences from accel2 at Mach 0.9.

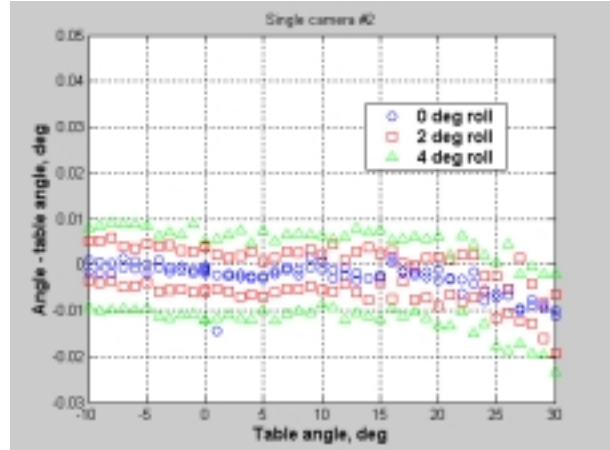


Figure 38. 1-camera solution of camera #2 with roll angles of  $0^\circ, \pm 2^\circ, \pm 4^\circ$ .

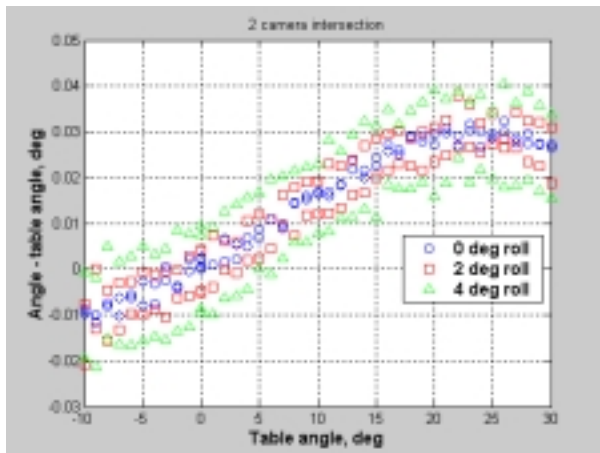


Figure 36. 2-camera intersection with roll angles of  $0^\circ, \pm 2^\circ, \pm 4^\circ$ .

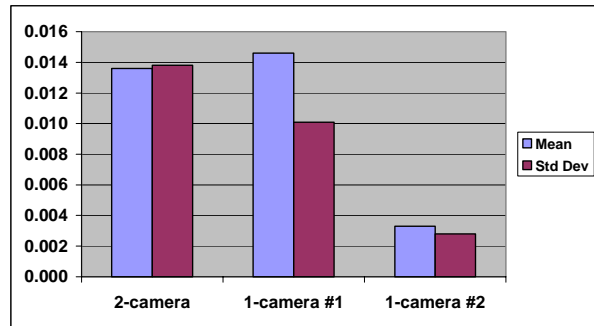


Figure 39. Error in degrees compared to indexing table for single camera and 2-camera photogrammetric reductions (without roll).

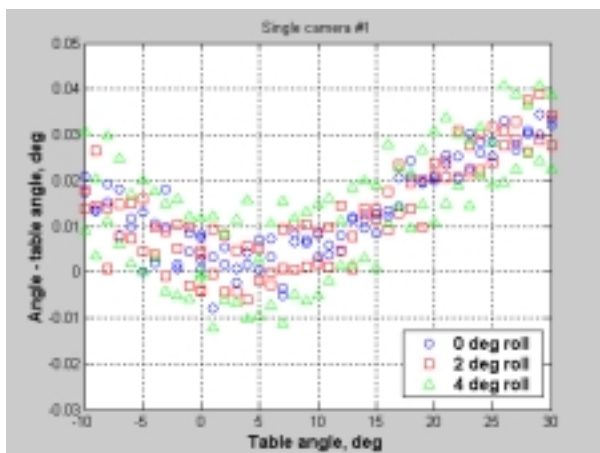


Figure 37. 1-camera solution of camera #1 with roll angles of  $0^\circ, \pm 2^\circ, \pm 4^\circ$ .

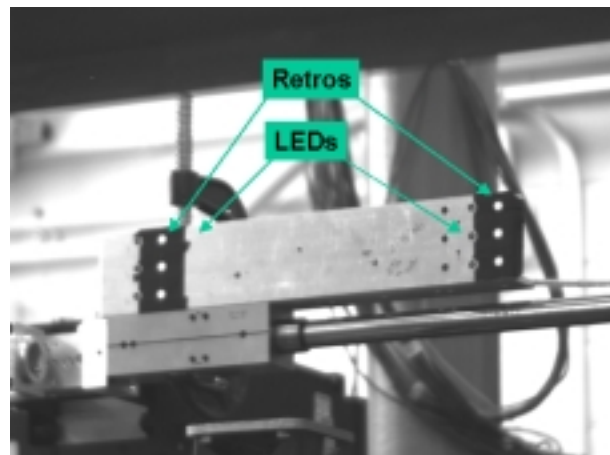


Figure 40. Plate containing LEDs used as active targets by Optotrak and retroreflective tape targets used as passive targets for the videogrammetric measurements during excitation from 0 to 70 Hz.

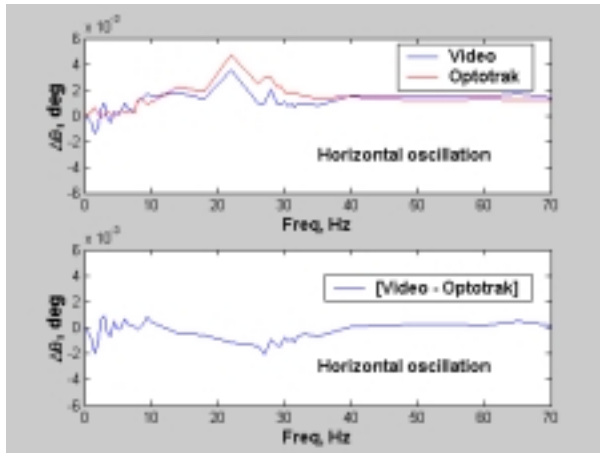


Figure 41. Change in angle as a function of horizontal oscillation frequency for videogrammetric and Optotrak angle measurements. Bottom plot is difference between video and Optotrak values.

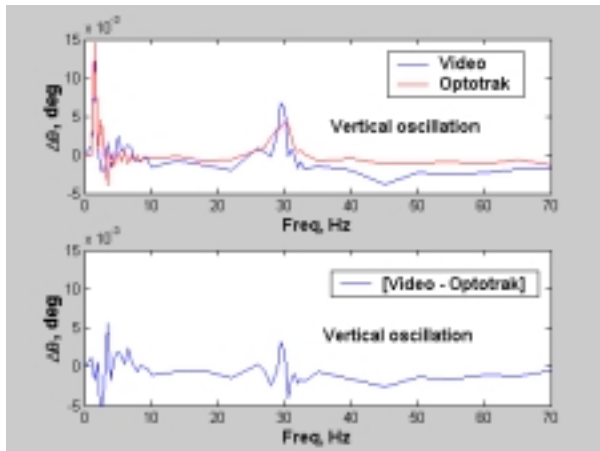


Figure 42. Change in angle as a function of vertical oscillation frequency for videogrammetric and Optotrak angle measurements. Bottom plot is difference between video and Optotrak values.